Preparation of C=C polymerization-oriented magnetic protein molecularly imprinted polymer and the application for membrane flux improvement

Qiming Zhang[a,c,1], Jiajun Hu[b,1], Hongcheng Guo [a,b], Chen Yang [a,b], Jixiang Li[a,c,*], Nan Liu[d], Wenshan Guo[e], Chaomeng Dai[f], Liang Wang[g], Yun Tian[h], Huu Hao Ngo[e,*]

[a] Shanghai Advanced Research Institute, Chinese Academy of Sciences, Shanghai 200120, China

[b] Shanghai Key Laboratory of Bio-Energy Crops, School of Life Sciences, Shanghai University, Shanghai 200444, China,

[c] University of Chinese Academy of Sciences, Beijing 100049, China

[d] Collaborative Innovation Center of Environmental Pollution Control and Ecological Restoration of Henan Province, Department of Material and Chemical Engineering, Zhengzhou University of Light Industry, Zhengzhou 450001, China

[e] School of Civil and Environmental Engineering, University of Technology Sydney, Sydney, NWS 2007, Australia

[f] College of Civil Engineering, Tongji University, Shanghai, 200092, China

[g] State Key Laboratory of Separation Membrane and Membrane Process, School of Environmental Science and Engineering, Tiangong University, Tianjin 300387, China

[h] Interdisciplinary Research Center for Sustainable Energy Science and Engineering (IRC4SE2), School of Chemical Engineering, Zhengzhou University, Zhengzhou, 450001, China

*Corresponding authors.

E-mail: lijixiang@sari.ac.cn (J.X., Li), HuuHao.Ngo@uts.edu.au (H.H. Ngo).

[1] Equal contribution.

Abstract:

This study aims to prepare a novel C=C polymerization-oriented magnetic protein molecularly imprinted polymer (MMIP) to improve membrane flux by adsorbing protein-type membrane foulants. The adsorption capabilities of MMIP were assessed by batch experiments, and the oriented polymerization and adsorption mechanisms were further revealed by density functional theory (DFT). The findings suggested that the MMIP exhibited a favorable adsorption capacity (35.9 mg/g) and high specificity (imprinting factor, IF=2.2) to bovine serum albumin (BSA), and showed an impressive adsorption capacity (21.2 mg/g) to protein-type substances in soluble microbial products (SMPs) derived from a functioning membrane bioreactor. Consequently, the MMIP reduced the filtration resistance by approximately 91.6% compared to the control group and improved the membrane flux. Moreover, the data confirmed that the adsorption was a monolayer adsorption process in which chemical interactions dominated the rate-limiting step. DFT calculations proved that the functional monomer chain reactions predominantly occurred on C=C bonds in the oriented polymerization and the hydrogen bonding was identified as the main interaction between MMIP and protein in the adsorption. These findings suggested that the MMIP holds great potential as a recyclable adsorbent for effectively improving membrane flux through the selective adsorption of protein-type membrane foulants.

Keywords: magnetic protein molecularly imprinted polymer, C=C oriented polymerization, membrane flux, density functional theory, hydrogen bonding

1. Introduction

It is well known that proteins, as the main substance of membrane foulants, significantly affect the membrane filtration processes (e.g., ultrafiltration (UF), nanofiltration (NF), reverse osmosis (RO), membrane bioreactor (MBR), *etc.*). Correspondingly, extensive methods have been executed to depress the production and amounts of proteins to sustain membrane filtration behaviors [1-5]. Among these methods, adding absorbents to adsorb the proteins is promising for membrane flux promotion because of its easy operation and fast effect [6-8]. For example, Liu et al. reported that powdered activated carbon could effectively increase the membrane flux by reducing the protein cake layer [9]. Chen et al. added granular activated carbon to treat dyeing wastewater, and they found that the adsorption of proteins significantly improved the RO membrane flux [10]. However, these adsorbents cannot adsorb foulants selectively, thereby having low protein adsorption efficiency and increasing the operation and maintenance costs [11, 12].

Unlike the adsorbents above, the magnetic molecularly imprinted polymer (MMIP) is an adsorbent with specific adsorption to specific substances [13]. Additionally, the MMIP has good physical and chemical stability, high specificity, easy separation and outstanding performance [14-17]. These render MMIP apply to several fields, such as solid-phase extraction, drug delivery, medical diagnostics, and environmental protection [18, 19]. Unfortunately, the current studies on MMIP using biomacromolecules as the templates such

as proteins, show unsatisfactory specific recognition ability owing to the significant impediments to mass transfer and the intricate structural composition [20]. Therefore, to obtain the desired biomacromolecule magnetic imprinted polymer (BMIP), the free radical polymerization (FRP) method was used to prepare BMIP [21-24]. For example, Xu et al. reported a novel MIP based on carbon-carbon double bond (C=C) functionalized nanoparticles for the exceptionally specific extraction of lysozyme[25], and the modification of C=C could effectively improve the adsorption capacity nearly twice [26, 27]. Besides, Zeng et al. developed a MIP with C=C selective directed polymerization on the SiO$_2$ shell surface for dopamine detection [28], and the modified C=C endowed MIP sensor a satisfactory detection limit in a wide linear range over dopamine concentration [29]. In a word, the copolymerization of C=C with functional monomers can guide the precise surface polymerization and improve the imprinting efficiency [30].

In this study, a novel C=C polymerization-oriented core-shell structure MMIP was prepared for specific adsorption of protein and its homologous substances to improve membrane permeate flux. The morphology and composition of MMIP were investigated by scanning electron microscope (SEM), Fourier transforms infrared spectrometry (FT-IR), vibrating sample magnetometer (VSM), energy dispersive x-ray spectroscopy (EDX), *etc*. Subsequently, the adsorption properties of MMIP such as capacity, selectivity, reusability, kinetics, thermodynamics and isotherms were systematically investigated. Further, the density functional theory (DFT) was used to elucidate the oriented polymerization and adsorption mechanisms. Finally, the effects of MMIP on filtration behaviors were evaluated. To the best

of our knowledge, this is the first study on using MMIP to specifically adsorb protein-based membrane foulants and improve membrane flux, and it is expected to provide deep insights into the oriented polymerization of MMIP and the effects of MMIP on membrane flux promotion.

2. Materials and methods

2.1. Materials

Bovine serum albumin (BSA, M_w = 66.4 kDa, pI = 4.9), Fe_3O_4 nanoparticles, sodium dodecyl sulfate (SDS), N, N-methylenebis acrylamide (MBA), N-Isopropyl acrylamide, tetraethyl orthosilicate (TEOS), acrylic acid, and N, N, N', N'-tetramethylethylenediamine (TEMED) were purchased by Adamas Reagent Co., Ltd (Shanghai, China). Absolute ethanol, ammonium hydroxide (NH$_3$·H$_2$O, 28%, w/w), acetic acid (HAc) and ammonium persulfate (APS) were sourced from Sinopharm Chemical Reagent Co., Ltd (Shanghai, China). The Polyvinylidene fluoride (PVDF) membranes were acquired from Shanghai Sinap Membranes Separation Technology Co., Ltd (Shanghai, China).

2.2. Preparation of MMIP

2.2.1. Preparation of $Fe_3O_4@SiO_2$

The Fe_3O_4 nanoparticles (NPs) were firstly suspended in 1 M HCl aqueous solution and ultrasonicated for 20 min, and then were washed with deionized water. The washed Fe_3O_4 was dispersed in a 200 mL mixed solvent system (ethanol: water = 4: 1, v/v) and thoroughly dispersed under ultrasonic conditions. Following, 10 mL NH$_3$·H$_2$O and 10 mL of TEOS were

added drop by drop and the reaction was stirred for 10 h at 25 °C. After that, the product was sufficiently washed with deionized water and dried under vacuum. Finally, the magnetic composite microspheres of $Fe_3O_4@SiO_2$ were obtained.

2.2.2. Preparation of MMIP

The $Fe_3O_4@SiO_2$ NPs (10 g) were firstly mixed with 200 mL ethyl alcohol, followed by adding 10 mL acrylic acid, and then reacted for 6 h at 25 °C. Finally, the magnetic composite microspheres of $Fe_3O_4@SiO_2@C=C$ were collected after repeated ethanol washing and vacuum-drying.

Secondly, the MMIP was prepared as follows: 1) BSA (2 g) as the template molecule, 2) N-isopropyl acrylamide (10 g) as the functional monomer, and 3) MBA (3 g) as the Cross-linker were mixed in 200 mL phosphate buffer saline (PBS, pH = 6.2, 10 mM). Afterward, 10 g magnetic composite microspheres of $Fe_3O_4@SiO_2@C=C$ were dispersed into the above solutions and shaken the mixture for 4 h at 25 °C. The APS and TEMED were then added to the solution and reacted under nitrogen protection for 24 h. Subsequently, the obtained product was alternately cleaned by water and 10 % (W/V) SDS-10 % (V/V) HAc solution to remove template molecules until the supernatant could not detect the absorption light of BSA by using UV-vis spectrophotometry, and the template elution step was completed. Ultimately, the core-shell MMIP was obtained after being vacuum-dried. The MNIP was the same as the MMIP preparation procedure but without adding the template proteins.

2.3. Characterization

BSA content was quantified by UV-vis spectrophotometer UV-4802S (Unico, China).

Soluble microbial products (SMPs) were obtained through a modified thermal extraction method [31]. Proteins and polysaccharides in SMPs were measured using the bicinchoninic acid assay (BCA) with BSA and anthrone method with glucose as a standard, respectively. Scanning Electronic Microscopy (SEM) was used to observe the morphology of adsorbents (Hitachi, Japan). Fourier Transform Infrared Spectroscopy (FT-IR) spectra in KBr were recorded on a Nicolet 380 (Thermal Fisher, USA). Vibrating Sample Magnetometer (VSM) was used to study the magnetic properties (Quantum Design, USA). The surface area tests were measured by Brunner-Emmet-Teller (BET, Micromeritics, USA). The filtration resistance was assessed by a terminal filtration system (SCM Ultrafiltration Cup, Sinap, China).

2.4. Batch tests

For the kinetic and thermodynamic experiments, the batch adsorption tests were conducted using BSA solutions. 50 mg of adsorbents and 10 mL BSA solution at the range of 0.2 - 1.6 mg/mL were mixed at different temperatures (25, 35 and 45 °C). After necessary incubation (15 - 720 min) and magnetic separation, the supernatant was immediately analyzed using a UV-vis spectrometer at 280 nm.

For the application experiment, the batch adsorption tests were carried out using SMPs derived from a functioning membrane bioreactor. 30 mg adsorbents were added into 150 mL SMPs solution and incubated at 25 °C. After incubation, the proteins in SMPs were immediately determined by the BCA method, and the polysaccharides were measured by the anthrone-sulfuric acid colorimetry method [32].

For the reusability experiment, four repeated adsorption-desorption experiments were performed to evaluate the regenerative property. Adsorption: 50 mg of adsorbents and 10 mL BSA solution at a concentration of 1.2 mg/mL were mixed at 25 ℃ for 120 min. Desorption: the adsorbed adsorbents were alternately eluted by water and 10 % (W/V) SDS-10 % (V/V) HAc solution for desorption until the elution could not detected BSA. The BSA concentration was also analyzed using a UV-vis spectrometer at 280 nm.

The adsorption capacity Q (mg/g) of MMIP or MNIP was calculated as follows:

$Q = (C_0 - C_e) V / m$ Eq. (1)

The imprinting factor (IF) was employed to assess the specificity of MMIP depending on the following equation [33]:

$IF = Q_{MMIP}/Q_{MNIP}$ Eq. (2)

2.5. DFT calculations

The DFT computations were calculated with Vienna Ab initio Simulation Package (VASP). Additionally, the electronic density of $Fe_3O_4@SiO_2@C=C$ nanoparticle was also calculated by using VASP. First, we constructed the structure of the materials. Since the exact structure of $Fe_3O_4@SiO_2$ was complicated, we replaced it with inert H to simplify the calculations. We then optimized the structure using VASP, and the resulting CONTCAR was converted to a new POSCAR for the next step of the calculation. In the next step, a static calculation was performed to obtain the charge density file CHGCAR. The VESTA software was used to process the file, which resulted in the charge distribution and two-dimensional charge density plot of C=C modified materials.

2.6. Determination of the membrane filtration resistance

The specific filtration resistance (SFR) was determined under a pressure of 0.03 MPa on a terminal filtration system which was composed of a 350 mL SCM ultrafiltration cup, a magnetic stirring paddle and a 32 cm^2 PVDF membrane. 30 mg MMIP or MNIP were introduced into 150 mL SMPs solution and mixed at 200 rpm. The weight of the permeate was determined on a balance. Furthermore, the filtration resistance was calculated as follows:

$$R = \frac{\triangle P}{\eta J} \quad \text{Eq. (3)}$$

Nomenclature			
C_0	initial of protein concentration (mg/mL)	K_2	pseudo-second-order rate constants (g/mg min)
C_e	equilibrium of protein concentration (mg/mL)	K_e	Elovich rate constants
V	volume of the initial protein solution (mL)	Ae	Elovich kinetics constant
m	quality of MMIP or MNIP in the sample (mg)	K_L	Langmuir model constants (L/mg)
Q_{MMIP}	adsorption capacities of MMIP (mg/g)	K_F	Freundlich constants
Q_{MNIP}	adsorption capacities of MNIP (mg/g)	n_F	Freundlich constants
R	filtration resistance (m^{-1})	α	adsorption enthalpy constants
η	kinematic viscosity (mPa·S)	β	capacity of the adsorbent constants
$\triangle P$	drop of pressure (Pa)	$\triangle$ $H^{\ominus}$	enthalpy change (kJ/mol)

J	permeate velocity (m^3/ (m^2·S))	$\triangle S^{\ominus}$	entropy change (J/mol K)
q_t	adsorption capacities at time t (min)	$\triangle$	Gibbs free energy change (kJ/mol)
		$G^{\ominus}$	
q_e	equilibrium adsorption capacities (mg/g)	K_D	equilibrium constants
q_m	maximum adsorption capacity (mg/g)	R	constant (8.314 J/mol K)
K_1	pseudo-first-order kinetics rate constants (L/mg)	T	absolute temperature (K)

*The definition and description of symbols in the formulae are uniformly listed in this table.

3. Results and discussion

3.1. Preparation

For the purpose of obtaining the desired MMIP, the C=C oriented polymerization was fulfilled according to scheme 1. Firstly, the Fe$_3$O$_4$ NPs were wrapped with SiO$_2$ to get the hybrid carriers of Fe$_3$O$_4$@SiO$_2$ NPs, which was beneficial to the subsequent functionalization and protected Fe$_3$O$_4$ NPs from aggregating and oxidating [34]. Secondly, the C=C monolayer was further introduced on the Fe$_3$O$_4$@SiO$_2$ using acrylic acid. Following, the functional monomers were oriented on the hybrid carriers of Fe$_3$O$_4$@SiO$_2$@C=C NPs by C=C directed polymerization. Meanwhile, the carboxyl group on BSA and the amine group on N-isopropyl acrylamide were bonded with hydrogen-bonding or covalent-bonding, allowing the template sites to be uniformly distributed on the polymer surface and improve the adsorption accessibility and adsorption rate. Similar reports have been documented by Kan et al. [35].

Finally, the template molecules were removed under acidic conditions by breaking the hydrogen-bonding or covalent-bonding [36], and the desired MMIP was obtained for use.
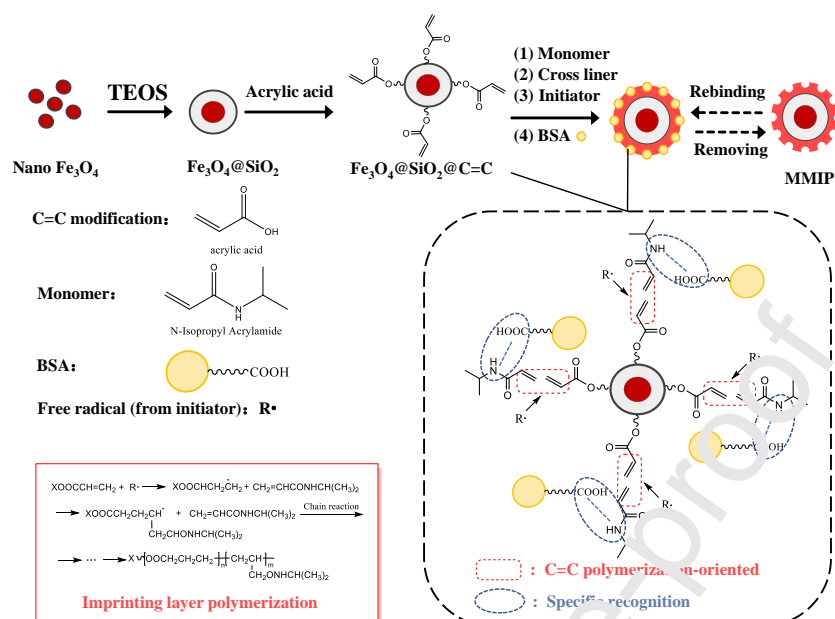
Scheme 1: Preparation and mechanism of C=C polymerization-oriented MMIP

Since the C=C-orientation played a crucial role in the preparation of MMIP, the charge distribution (Fig. 2a) and charge density (Fig. 2b) of $Fe_3O_4@SiO_2@C=C$ were investigated to elucidate the directional mechanism by DFT. It is evident from Fig. 2b that the charge density of oxygen-containing groups (0.4), such as carbonyl, carboxyl, and hydroxyl groups, was higher than that of C=C (0.34), which was due to the free radicals preferentially attack functional groups with high charge density [37]. However, the electronegativity of oxygen atom enabled it to attract the surrounding electrons more strongly (particularly the shared electron pairs), leading to a significant electron cloud polarization effect [38]. The charge distribution of oxygen-containing groups stabilized the shared electrons, and the oxygen-containing groups were less likely to be attacked by free radicals compared to C=C bonds.

Consequently, the chain polymerization reactions initiated by free radicals mainly occurred on C=C bonds, producing the desired MMIP.
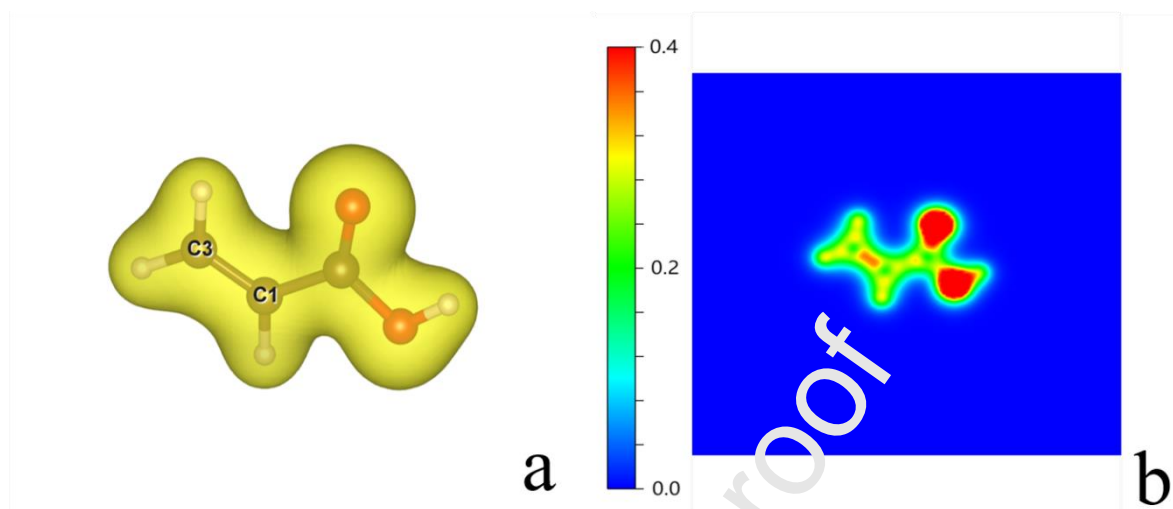

Fig. 1: Charge distribution (a) and charge density (b) of $Fe_3O_4@SiO_2@C=C$ (In order to simplify the calculations, we replaced the hybrid carrier of $Fe_3O_4@SiO_2$ with inert H, C1 and C3 represent the two carbon atoms in C=C bond, red represents O, white represents H, and black represents C.)

3.2. Characterization

3.2.1. SEM and BET

The surface morphologies of Fe_3O_4, $Fe_3O_4@SiO_2$, MMIP and MNIP were characterized by SEM (Fig. 2). It could be observed that the Fe_3O_4 NPs had a uniform particle size of around 30 nm (Fig. 2a). After silica coating, the particle size of $Fe_3O_4@SiO_2$ NPs (Fig. 2b) increased significantly and shaped as agglomerate spheres with smooth surfaces. After oriented polymerization, the MMIP and MNIP (Fig. 2c and Fig. 2d) were well prepared and shaped as more porous agglomerates with rough surfaces.
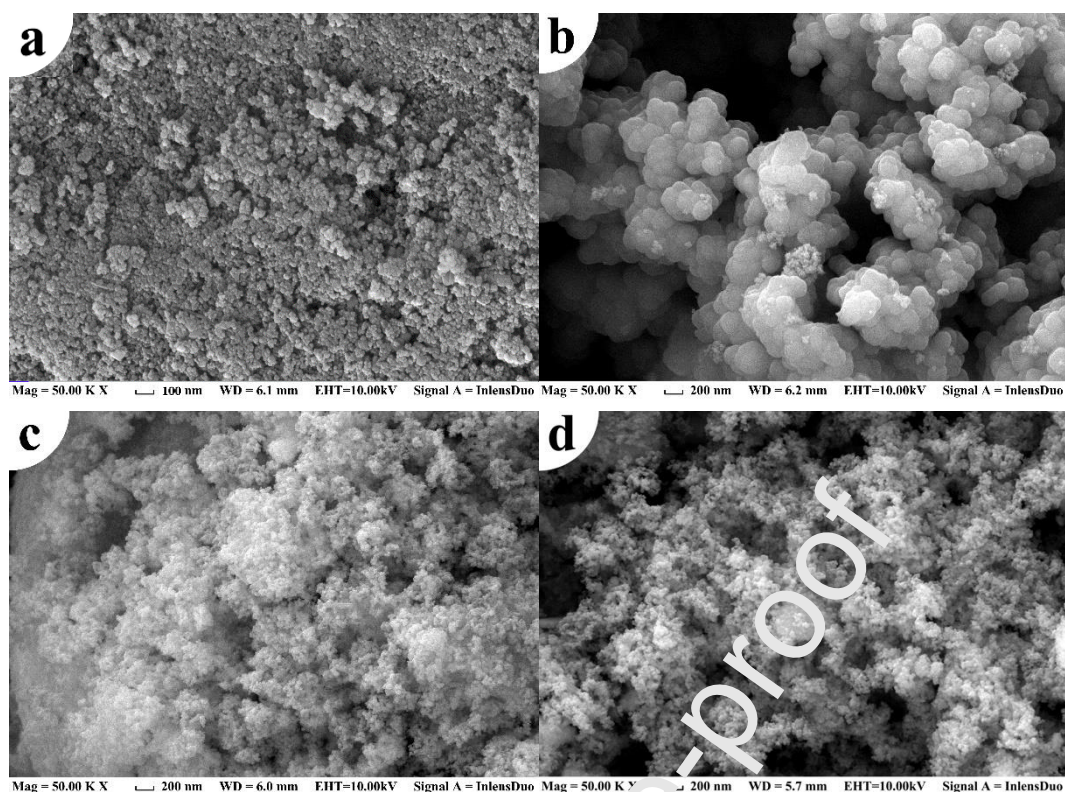
Fig. 2: SEM images of Fe$_3$O$_4$ (a), Fe$_3$O$_4$@SiO$_2$ (b), MMIP (c) and MNIP (d). Experimental conditions: Mag = 50 KX, EHT = 10.00 KV.

Also, the BET specific surface areas of Fe$_3$O$_4$, MMIP and MNIP were measured using N$_2$ adsorption-desorption method. It can be seen from Fig. 3 that all the N$_2$ physisorption isotherms presented an adsorption hysteresis loop belonging to isotherm IV [39], suggesting the presence of mesopores (2-50 nm) in the polymers. Moreover, the BET surface area of MMIP (94.28 m²/g) was higher than that of MNIP (86.22 m²/g) and Fe$_3$O$_4$ (65.33 m²/g), which might be attributed to the imprinting cavities of MMIP. These morphological characteristics facilitated more binding sites, producing the higher adsorption capacities for MMIP.
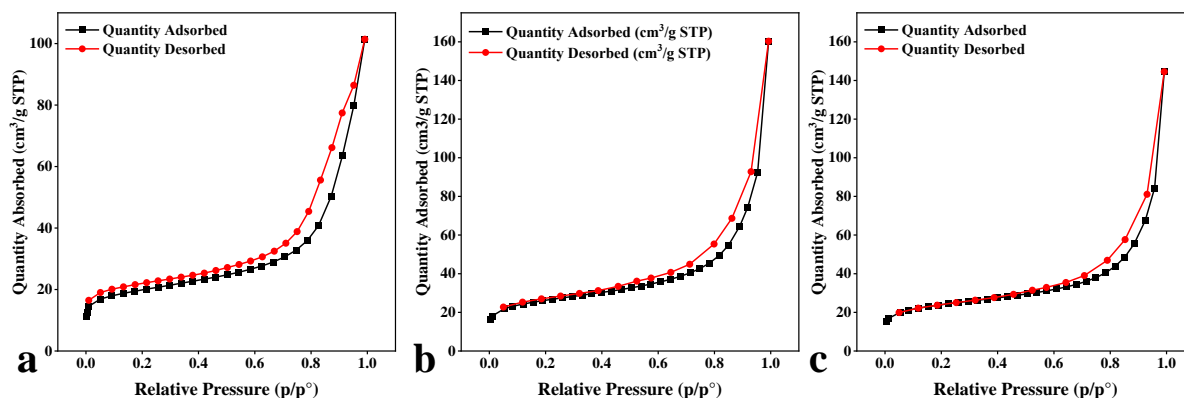
Fig. 3: The N_2 physisorption isotherms of Fe_3O_4 (a), MMIP (b) and MNIP (c)

3.2.2. FT-IR and EDX

The chemical compositions of carriers, MMIP and MNIP were identified by FT-IR, and the results are illustrated in Fig. 4b. The peaks at 562 cm^{-1} and 634 cm^{-1} were assigned to the Fe-O stretching vibration. The peaks at 797 cm^{-1} and 1082 cm^{-1} were assigned to the bending vibration and stretching vibration of Si-O-Si, respectively, suggesting that the SiO_2 is successfully coated on the Fe_3O_4 NPs. Moreover, two characteristic absorption peaks of -COOH at 1402 cm^{-1} and 932 cm^{-1} appeared on the $Fe_3O_4@SiO_2$ but not for the $Fe_3O_4@SiO_2@C=C$, proving that the -COOH was introduced when coating silica, which has a significant impact on the subsequent functional C=C modification. Additionally, the shapes of FT-IR spectra of MMIP and MNIP in Fig. 4c confirmed that the peak at 1698 cm^{-1} of C=C disappeared, indicating the functional monomer was polymerized by C=C orientation. Besides, the MMIP and MNIP had the same shape of FT-IR spectra, suggesting the complete removal of protein templates.

EDX was also used to study the elemental composition of MMIP (Fig. 4a), and the

elements of Fe, O, C, and Si in MMIP were 42.3%, 34.1%, 14.0%, and 9.0%, respectively. The EDX results reconfirmed: (1) The Fe_3O_4 NPs were the main component of MMIP and fabricated its fast separation; (2) The SiO_2 layers were successfully coated and benefitted the sequent functionalization, simultaneously, protecting the Fe_3O_4 NPs from aggregating and oxidating; (3) The organic imprinting layers were successfully polymerized in MMIP.
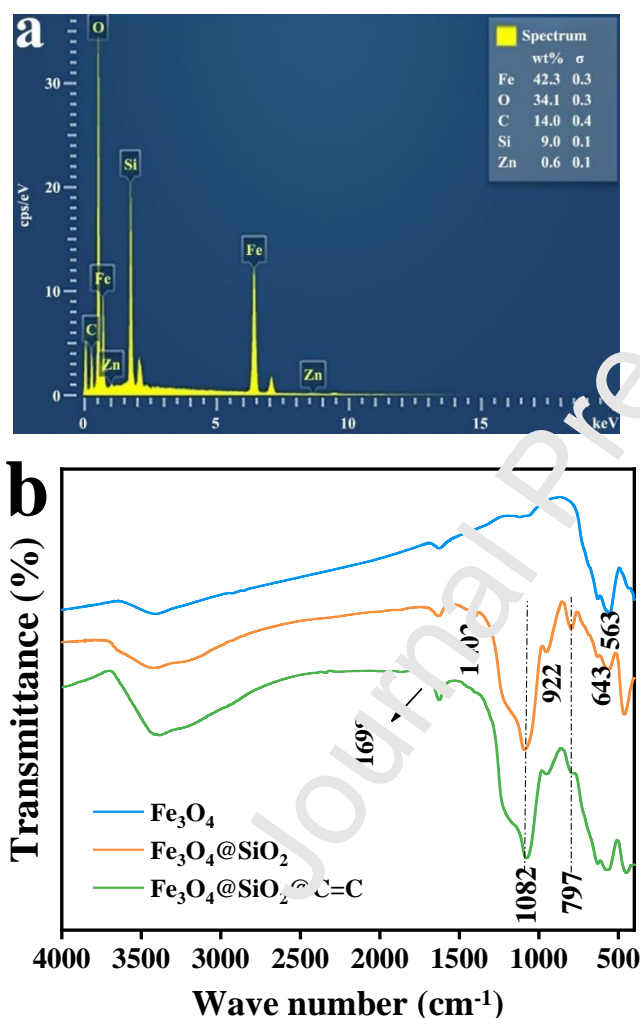
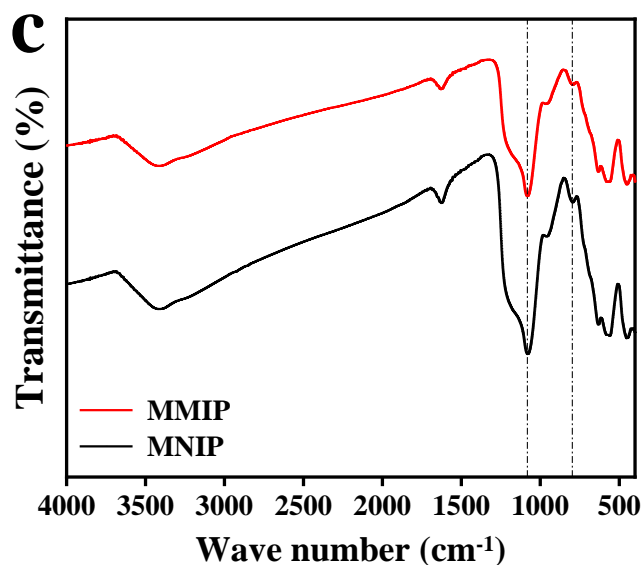Fig. 4: EDX of MMIP (a), FT-IR spectra of Fe_3O_4, $Fe_3O_4@SiO_2$, and $Fe_3O_4@SiO_2@C=C$ (b), FT-IR spectra of MMIP and MNIP (c)

3.2.3. Magnetic properties analysis

The magnetic properties of Fe_3O_4, MMIP and MNIP were characterized using VSM. As illustrated in Fig. 5, their saturation magnetization values were 63.12, 47.13 and 49.52 emu/g, respectively. Also, there were no remanence and coercivity of them, indicating that they were all super-magnetic. Compared with Fe_3O_4, the MMIP exhibited a reduction in saturation magnetization by approximately 15.99 emu/g due to the presence of the silica coating. Similar results were reported by Zhang et al. [40, 41], and they found that the saturation magnetization of 14.8 emu/g enabled the rapid separation of Lyz-MMIP from aqueous solution by an external magnetic field within 30 s. Therefore, the saturation magnetization of 47.13 emu/g was sufficient for MMIP to be separated from complex environments in practical engineering applications.
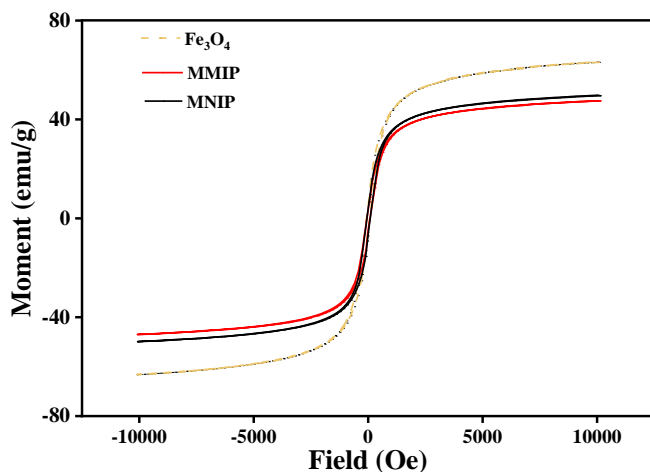
Fig. 5: Magnetic hysteresis loops of Fe_3O_4, MMIP and MNIP

3.3. Adsorption kinetics

The effect of time on the adsorption of BSA on MMIP and MNIP is given in Fig. 6. Fast adsorption of both polymers initially occurred within 0-30 min, then slowed down from 30-120 min, and finally reached equilibrium. The initial fast adsorption rate was due to the numerous unoccupied adsorption sites on the MMIP. With the adsorption sites gradually occupied by BSA, the adsorption rate decreased until the adsorption reached equilibrium. The equilibrium adsorption capacity of MMIP to BSA reached approximately 35.90 mg/g, significantly surpassing that of MNIP (16.30 mg/g). This difference can be attributed to the abundant specific adsorption sites on MMIP.
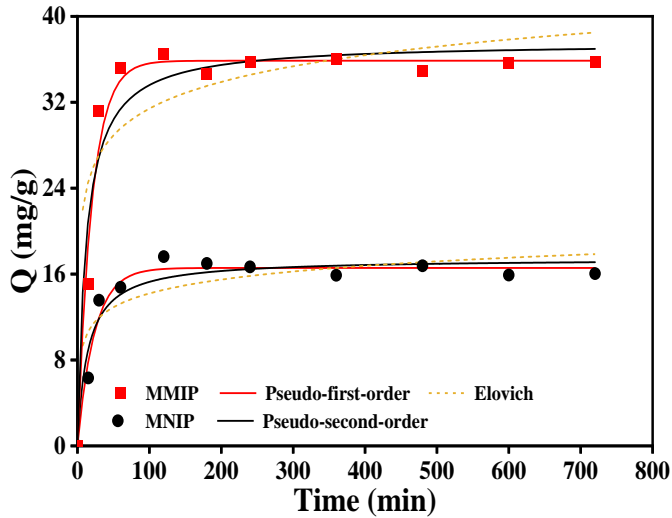
Fig. 6: The kinetic curves of BSA adsorption on MMIP and MNIP. Experimental conditions: 50 mg of MMIP or MNIP were added in 10 mL of BSA phosphate buffer (pH = 6.2, 10 mM) at a concentration of 1.2 mg/mL, and then were incubated at 25 °C.

Kinetic studies are crucial due to the valuable information they can reveal about adsorption rate and adsorption mechanism [42, 43]. The kinetic adsorption data were investigated using Pseudo-first-order, Pseudo-second-order and Elovich models. The models were described as follows:

Pseudo-first-order: $\ln(q_e - q_t) = \ln q_e - K_1 t$ Eq. (4)

Pseudo-second-order: $\dfrac{t}{q_t} = \dfrac{1}{K_2 q_e^2} + \dfrac{t}{q_e}$ Eq. (5)

Elovich: $q_t = K_e \ln t + A_e$ Eq. (6)

The kinetic parameters were calculated and presented in Table 1. It can be found that the pseudo-second-order model fitted better with the experiment data in sync with the best q_e values, suggesting that the chemical interaction between BSA and MMIP was probably the rate-limiting step and dominated the adsorption reaction. The detailed adsorption mechanism

will be further discussed by DFT in section 3.7.

Table 1: The kinetic parameters of BSA adsorption on MMIP and MNIP

Adsorbent	Pseudo-first-order model			Pseudo-second-order model			Elovich model		
	q_e (mg/g)	K_1 (L/mg)	R^2	q_e (mg/g)	K_2 (g/mg min)	R^2	A_e	K_e	R^2
MMIP	35.86	0.0498	0.976	35.90	0.0056	0.999	14.86	3.5925	0.856
MNIP	16.56	0.0426	0.971	16.30	0.0245	0.998	5.64	1.8563	0.841

..

3.4. Adsorption isotherms

The adsorption effects of MMIP and MNIP on BSA at different concentrations were evaluated and shown in Fig. 7. Both adsorption curves of MMIP and MNIP showed a sharp increase followed by a gradual plateau. The saturated BSA adsorption capacities of MMIP and MNIP reached approximately 35.90 mg/g and 16.30 mg/g, respectively. In other words, it is stated that the adsorption of MMIP for BSA is selective (IF_{BSA}=2.2). It may be aroused by the weak chemical interaction between MMIP and BSA. The specific adsorption mechanism will be comprehensively below revealed by DFT calculations.

The adsorption data were further fitted using Langmuir, Freundlich and Temkin models, and the parameters calculated from isotherm models were listed in Table 2.

Langmuir: $\dfrac{1}{q_e} = \dfrac{1}{K_L q_m C_e} + \dfrac{1}{q_m}$ Eq. (7)

Freundlich: $q_e = K_F C_e^{\frac{1}{n_F}}$ Eq. (8)

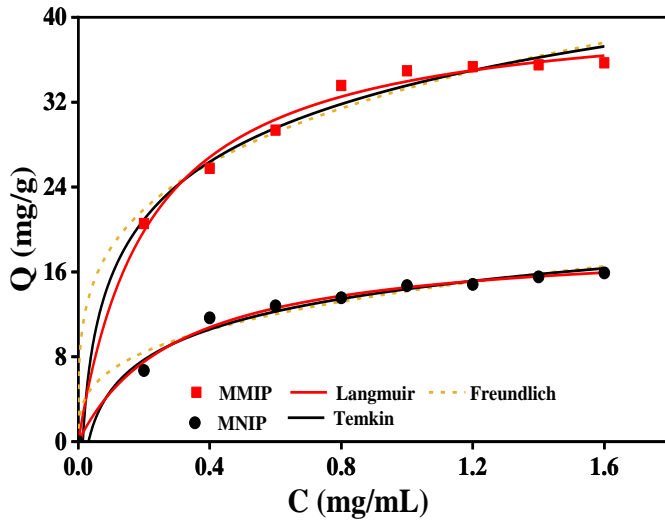**Temkin: $q_e = \alpha \ln \beta + \alpha \ln C_e$**   Eq. (9)

Fig. 7: The adsorption isotherms of BSA on MMIP and MNIP. Experimental conditions: 50 mg of MMIP or MNIP were added in 10 mL of BSA phosphate buffer (pH = 6.2, 10 mM) at a range of 0.2 - 1.6 mg/mL for 120 min, and then were incubated at 25 °C.

Table 2: The isotherm parameters of BSA adsorption on MMIP and MNIP

Adsorbent	Langmuir model			Freundlich model			Temkin model		
	q_m (mg/g)	K_L (L/mg)	R^2	K_F	n_F	R^2	α	β	R^2
MMIP	36.90	12.182	0.941	33.37	3.589	0.953	7.846	72.15	0.961
MNIP	18.45	4.0148	0.972	14.28	2.641	0.893	4.147	32.13	0.953

..

It can be observed from Table 2 that the Temkin model ($R^2 = 0.961$) fitted much better with the experiment data of MMIP than other models. Since the Temkin isotherm is derived from the Langmuir isotherm, it is stated that the adsorption process was a monolayer adsorption, and occurred on the surface of adsorbents. Additionally, the adsorption heat decreased linearly with the adsorption amount increasing, and the binding energy was uniformly

distributed. Moreover, the higher β value of MMIP, which was considered as a constant related to the adsorption potential in Temkin model, indicated a stronger adsorbent-adsorbate interaction between MMIP and BSA [44, 45].

3.5. Adsorption thermodynamics

The effect of temperature (from 25 to 45 ℃) on BSA adsorption by MMIP and MNIP was investigated, and the thermodynamic parameters such as $\triangle H^{\Theta}$, $\triangle S^{\Theta}$ and $\triangle G^{\Theta}$ were calculated through Eq. (10)-Eq. (10). The results were summarized in Table 3.

$$K_D = \frac{q_e}{C_e} \qquad \text{Eq. (10)}$$

$$\ln K_D = -\frac{\triangle H^{\Theta}}{RT} + \frac{\triangle S^{\Theta}}{R} \qquad \text{Eq. (11)}$$

$$\triangle G^{\Theta} = \triangle H^{\Theta} - T \triangle S^{\Theta} \qquad \text{Eq. (12)}$$

Table 3: The thermodynamic parameters of BSA adsorption on MMIP and MNIP

	T (°C)	q_e (mg/g)	K_D	$\triangle H^{\Theta}$ (kJ/mol)	$\triangle S^{\Theta}$ (J/mol K)	$\triangle G^{\Theta}$ (kJ/mol)
MMIP	25	35.0	42.42	10.15	65.21	-9.291
	35	39.0	49.447			-9.943
	45	42.6	54.330			-10.595
MNIP	25	15.0	16.216	8.379	51.27	-6.907
	35	16.6	18.103			-7.419
	45	20.2	22.469			-7.932

..

Experimental conditions: 50 mg of MMIP or MNIPs were added in 10 mL of BSA phosphate buffer (pH = 6.2, 10 mM) at a concentration of 1.2 mg/mL for 120 min, and then were incubated at 25, 35 and 45 ℃.

It can be seen from Table 3 that the adsorption capacities of MMIP and MNIP both exhibited an upward trend as the temperature increasing, indicating the BSA adsorption on MMIP or MNIP was an endothermic process. The negative values of $\triangle G^{\ominus}$ indicated that the BSA adsorption on MMIP or MNIP was spontaneous. A lower $\triangle G^{\ominus}$ was obtained at a higher temperature, suggesting the higher temperature was more conducive to the adsorption. The positive $\triangle H^{\ominus}$ value also revealed that the adsorption process was endothermic. Additionally, a positive $\triangle S^{\ominus}$ value suggested an increase in randomness at the interfaces between the adsorbent and adsorbate.

3.6. The reusability of MMIP

In order to test the reusability of MMIP, four repeated adsorption-desorption experiments were performed and the results were provided in Fig. 8. It was noticed that the adsorption capacity of MMIP remained approximately 88.49% even after four successive recycles. The marginal decrease of 11.51% may be aroused by the breakdown or block of a few binding sites [46]. Additionally, the SiO_2 layers could protect the Fe_3O_4 NPs from aggregating and oxidating, and the MMIP could also be rapidly separated and recovered by an external magnetic field after four cycles of adsorption-desorption. These findings proved that the MMIP had great potential for practical applications.
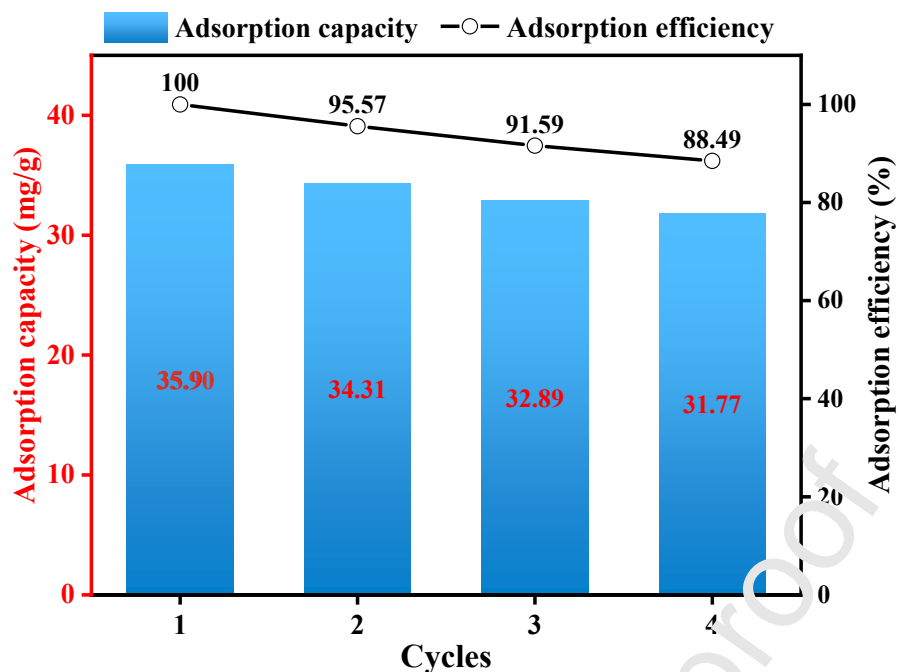
Fig. 8: Reusability of MMIP. Experimental conditions: 50 mg of MMIP or MNIP were added in 10 mL of BSA phosphate buffer (pH = 6.2, 10 mM) at a concentration of 1.2 mg/ mL , and then were incubated at 25 ℃ for 120 min.

3.7. The adsorption mechanisms by DFT

The adsorption mechanisms between MMIP and protein were further revealed by DFT calculations. As illustrated in Fig. 9a, the five possible interaction pathways were proposed, and the corresponding binding energy values were calculated (Fig. 9b). It could be observed that the pathway 5 exhibited a significantly positive binding energy value, stating that there was a lower likelihood of forming covalent-bonding between carboxyl group on protein and amine group on MMIP. On the other hand, the binding energy values of hydrogen bonds from pathways 1, 2, 3 and 4 were all negative, demonstrating the thermodynamic feasibility of forming these four types of hydrogen bonds. Moreover, the binding energy of pathway 3 was

the lowest, and simultaneously formed two hydrogen bonds between protein and MMIP, which could be assumed that the binding mechanism of MMIP to protein was dominated by hydrogen-bonding, as well as potentially formed multiple hydrogen bonds between the molecules. This conclusion was consistent with Liu et. al [47].
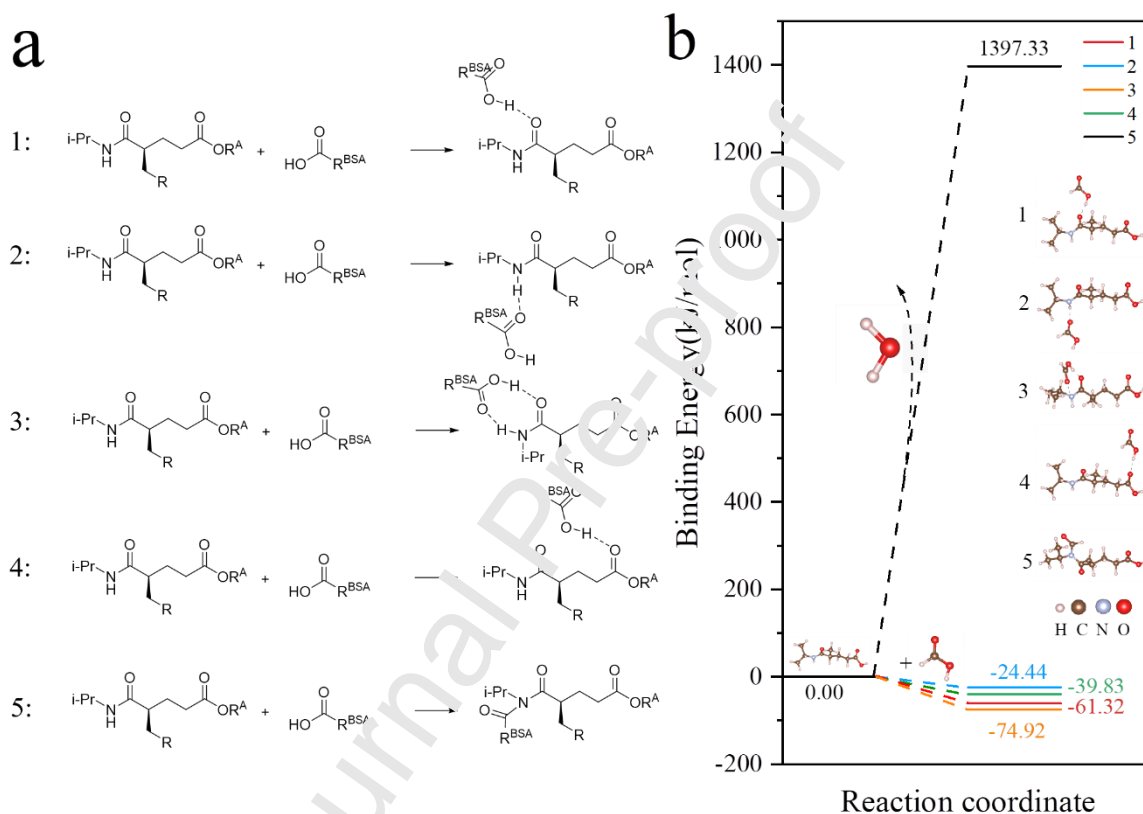

Fig. 9: The five possible interaction pathways and binding energy values between MMIP and protein (i-Pr represents isopropyl, ORA represents the $Fe_3O_4@SiO_2$, RBSA represents the simplified protein structure)

3.8. Evaluation of membrane permeate flux

Selective adsorption tests were further conducted to evaluate the applicability of MMIP on SMPs reduction and the effects on membrane filtration resistance, and the results are shown

in Fig. 10. It can be seen from Fig. 10a that the adsorption capacities of MMIP and MNIP to

protein were 21.2 mg/g and 12.4 mg/g, respectively. Obviously, the MMIP exhibited much

higher selectivity for protein-type substances ($IF_{protein}$=1.71) and similarly lower capacity for

polysaccharide-type substances than that of MNIP. As revealed by DFT, the high and specific

adsorption capacity of MMIP for protein might be attributed to hydrogen-bonding, and the

non-specific adsorption of polysaccharide was aroused by electrostatic incorporation. As a

result, the non-specific adsorption of polysaccharide and the specific adsorption of protein

facilitated MMIP in effectively decreasing membrane resistance and improving membrane

flux. Compared to the control group of SMPs, the filtration resistance of MMIP was reduced

by 91.6%, while the filtration resistance of MNIP was only reduced by 72.3%. In other words,

the MMIP could effectively improve 91.6% of membrane flux. These results confirmed that

the specific adsorption of MMIP for protein could effectively reduce protein-type membrane

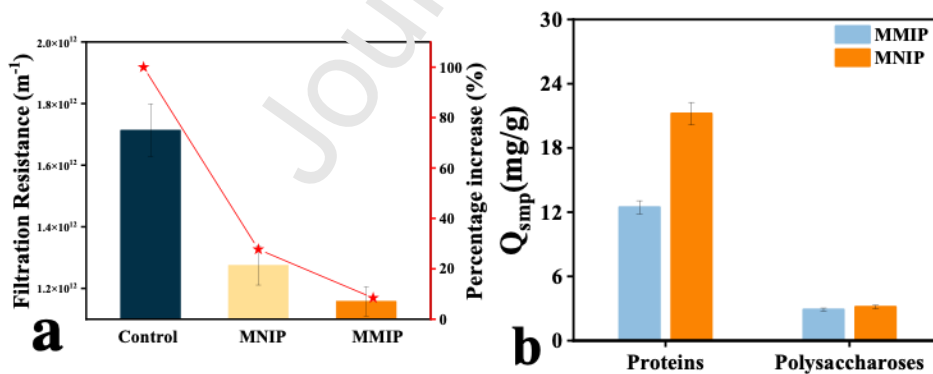fouling and improve membrane permeate flux.

Fig. 10: The adsorption capacities of MMIP and MNIP to SMPs (a) and the effect on filtration

resistance (b). Experimental conditions: 30 mg of MMIP or MNIP were added into 150 mL

SMP solution and incubated at 25 °C, and the terminal filter was determined under 0.03 MPa

at 200 rpm.

4. Conclusion

In this study, a novel C=C polymerization-oriented core-shell MMIP was successfully prepared and applied to enhance membrane flux through selective adsorption of protein-type foulants. The main findings are shown below: (1) Specific adsorption capacity: The C=C-oriented polymerization of the imprinting layer could endow MMIP with a good specific adsorption capacity for BSA (35.9 mg/g, IF = 2.2) and a high adsorption to homologous proteins from SMPs (21.2 mg/g); (2) Membrane flux improvement: The SFR tests proved the MMIP could significantly promote the membrane flux; (3) Adsorption mechanisms: The chemical interaction was the rate-limiting step, and DFT calculations revealed that the hydrogen-bonding contributed to the adsorption of MMIP to protein. The results obtained from this study confirmed that the MMIP had the ability to reduce protein-type membrane fouling and improved membrane permeate flux effectively.

Data availability

Data will be made available on request.

References

[1] B. Gong, W. Chen, C. Qian, P.H.L. Sit, X.W. Liu, H.Q. Yu, Contribution of proteins to ceramic membrane fouling at the early stage of membrane filtration, Separation and Purification Technology 312 (2023). https://doi.org/10.1016/j.seppur.2023.123450.

[2] Y.C. Lin, K.M. Liu, C.M. Chao, D.K. Wang, K.L. Tung, H.H. Tseng, Enhanced anti-protein fouling of PVDF membrane via hydrophobic-hydrophobic adsorption of styrene-terminated amphiphilic linker, Chemical Engineering Research & Design 156 (2020) 273-280. https://doi.org/10.1016/j.cherd.2020.02.005.

[3] G.Q. Chen, Y.H. Wu, P.S. Fang, Y. Bai, Z. Chen, Y.Q. Xu, Y.H. Wang, X. Tong, L.W. Luo, H.B. Wang, Z.W. Zhang, N. Ikuno, H.Y. Hu, Performance of different pretreatment methods on alleviating reverse osmosis membrane fouling caused by soluble microbial products, Journal of Membrane Science 641 (2022). https://doi.org/10.1016/j.memsci.2021.119850.

[4] T. Miyoshi, Y. Nagai, T. Aizawa, K. Kimura, Y. Watanabe, Proteins causing membrane fouling in membrane bioreactors, Water Sci Technol 72(6) (2015) 844-849. https://doi.org/10.2166/wst.2015.282.

[5] M. Aslam, F. Wicaksana, M. Farid, A. Wong, W.B. Krantz, Mitigation of membrane fouling by whey protein via water hammer, Journal of Membrane Science 642 (2022). https://doi.org/10.1016/j.memsci.2021.119967.

[6] X.Z. Zhao, H.X. Xuan, Y.L. Chen, C.J. He, Preparation and characterization of superior antifouling PVDF membrane with extremely ordered and hydrophilic surface layer, J Membr

Sci 494 (2015) 48-56. https://doi.org/10.1016/j.memsci.2015.07.052.

[7] J. Xiong, S. Yu, Y. Hu, Y. Yang, X.C. Wang, Applying a dynamic membrane filtration (DMF) process for domestic wastewater preconcentration: Organics recovery and bioenergy production potential analysis, Sci Total Environ 680 (2019) 35-43. https://doi.org/10.1016/j.scitotenv.2019.05.080.

[8] H. Hazrati, N. Jahanbakhshi, M. Rostamizadeh, Fouling reduction in the membrane bioreactor using synthesized zeolite nano-adsorbents, J Memb Sci 555 (2018) 455-462. https://doi.org/10.1016/j.memsci.2018.03.076.

[9] J. Liu, J. Tian, Z. Wang, D. Zhao, F. Jia, B. Dong, Mechanism analysis of powdered activated carbon controlling microfiltration membrane fouling in surface water treatment, Colloids and Surfaces A: Physicochemical and Engineering Aspects 517 (2017) 45-51. https://doi.org/https://doi.org/10.1016/j.colsurfa.2017.01.009.

[10] G.Q. Chen, Y.H. Wu, Y.J. Tan, Z. Chen, X. Tong, Y. Bai, L.W. Luo, H.B. Wang, Y.Q. Xu, Z.W. Zhang, N. Ikuno, H.Y. Hu, Pretreatment for alleviation of RO membrane fouling in dyeing wastewater reclamation, Chemosphere 292 (2022). https://doi.org/10.1016/j.chemosphere.2021.133471.

[11] Y. Xiao, H. Waheed, K. Xiao, I. Hashmi, Y. Zhou, In tandem effects of activated carbon and quorum quenching on fouling control and simultaneous removal of pharmaceutical compounds in membrane bioreactors, Chem Eng J 341 (2018) 610-617. https://doi.org/https://doi.org/10.1016/j.cej.2018.02.073.

[12] F. Parveen, N. Hankins, Comparative performance of nanofiltration and forward osmosis

membranes in a lab-scale forward osmosis membrane bioreactor, Journal of Water Process Engineering 28 (2019) 1-9. https://doi.org/https://doi.org/10.1016/j.jwpe.2018.12.003.

[13] A.A. Lahcen, A.A. Baleg, P. Baker, E. Iwuoha, A. Amine, Synthesis and electrochemical characterization of nanostructured magnetic molecularly imprinted polymers for 17-β-Estradiol determination, Sensors and Actuators B: Chemical 241 (2017) 698-705. https://doi.org/https://doi.org/10.1016/j.snb.2016.10.132.

[14] H. Guo, J. Hu, J. Li, M.-t. Gao, Q. Wang, W. Guo, H.H. Ngo, Systematic insight into the short-term and long-term effects of magnetic microparticles and nanoparticles on critical flux in membrane bioreactors, Journal of Membrane Science 582 (2019) 284-288. https://doi.org/10.1016/j.memsci.2019.04.015.

[15] Y. Liu, J. Li, W. Guo, H.H. Ngo, J. Hu, M.-t. Gao, Use of magnetic powder to effectively improve the performance of sequencing batch reactors (SBRs) in municipal wastewater treatment, Bioresource Technology 248 (2018) 135-139. https://doi.org/10.1016/j.biortech.2017.06.069.

[16] J. Zhou, Y. Wang, J. Bu, B. Zhang, Q. Zhang, Ni2+-BSA Directional Coordination-Assisted Magnetic Molecularly Imprinted Microspheres with Enhanced Specific Rebinding to Target Proteins, ACS Applied Materials & Interfaces 11(29) (2019) 25682-25690. https://doi.org/10.1021/acsami.9b06507.

[17] K. Xu, Y. Wang, X. Wei, J. Chen, P. Xu, Y. Zhou, Preparation of magnetic molecularly imprinted polymers based on a deep eutectic solvent as the functional monomer for specific recognition of lysozyme, Microchimica Acta 185(2) (2018) 146.

https://doi.org/10.1007/s00604-018-2707-8.

[18] Y. Zhang, Y. Lu, J. Zhong, W. Li, Q. Wei, K. Wang, Molecularly imprinted polymer microspheres prepared via the two-step swelling polymerization for the separation of lincomycin, Journal of Applied Polymer Science 136(37) (2019) 47938. https://doi.org/10.1002/app.47938.

[19] A. Özkan, N. Atar, M.L. Yola, Enhanced surface plasmon resonance (SPR) signals based on immobilization of core-shell nanoparticles incorporated boron nitride nanosheets: Development of molecularly imprinted SPR nanosensor for anticancer drug, etoposide, Biosensors and Bioelectronics 130 (2019) 293-298. https://doi.org/https://doi.org/10.1016/j.bios.2019.01.053.

[20] M. Dinc, C. Esen, B. Mizaikoff, Recent advances on core–shell magnetic molecularly imprinted polymers for biomacromolecules, TrAC Trends in Analytical Chemistry 114 (2019) 202-217. https://doi.org/10.1016/j.trac.2019.03.008.

[21] P. Zahedi, M. Ziaee, M. Abdouss, A. Farazin, B. Mizaikoff, Biomacromolecule template-based molecularly imprinted polymers with an emphasis on their synthesis strategies: a review, Polym Adv Technol 27(9) (2016) 1124-1142. https://doi.org/10.1002/pat.3754.

[22] S. Huang, J. Xu, J. Zheng, F. Zhu, L. Xie, G. Ouyang, Synthesis and application of magnetic molecularly imprinted polymers in sample preparation, Anal Bioanal Chem 410(17) (2018) 3991-4014. https://doi.org/10.1007/s00216-018-1013-y.

[23] L. Ye, Synthetic Strategies in Molecular Imprinting, in: B. Mattiasson, L. Ye (Eds.), Molecularly Imprinted Polymers in Biotechnology2015, pp. 1-24.

https://doi.org/10.1007/10_2015_313.

[24] V.D. Salian, M.E. Byrne, Living Radical Polymerization and Molecular Imprinting: Improving Polymer Morphology in Imprinted Polymers, Macromolecular Materials and Engineering 298(4) (2013) 379-390. https://doi.org/10.1002/mame.201200191.

[25] W. Xu, Q.Z. Dai, Y.Z. Wang, X.J. Hu, P.L. Xu, R. Ni, J.J. Meng, Creating magnetic ionic liquid-molecularly imprinted polymers for selective extraction of lysozyme, Rsc Advances 8(39) (2018) 21850-21856. https://doi.org/10.1039/c8ra03818j.

[26] H. Duan, X. Wang, Y. Wang, Y. Sun, J. Li, C. Luo, An ultrasensitive lysozyme chemiluminescence biosensor based on surface molecular imprinting using ionic liquid modified magnetic graphene oxide/beta-cyclodextrin as supporting material, Analytica Chimica Acta 918 (2016) 89-96. https://doi.org/10.1016/j.aca.2016.03.008.

[27] K. Xu, Y. Wang, X. Wei, J. Chen, P. Xu, Y. Zhou, Preparation of magnetic molecularly imprinted polymers based on a deep eutectic solvent as the functional monomer for specific recognition of lysozyme, Microchimica Acta 185(2) (2018). https://doi.org/10.1007/s00604-018-2707-8.

[28] Y.B. Zeng, Y. Zhou, L. Kong, T.S. Zhou, G.Y. Shi, A novel composite of SiO2-coated graphene oxide and molecularly imprinted polymers for electrochemical sensing dopamine, Biosensors & Bioelectronics 45 (2013) 25-33. https://doi.org/10.1016/j.bios.2013.01.036.

[29] Y. Mao, Y. Bao, S. Gan, F. Li, L. Niu, Electrochemical sensor for dopamine based on a novel graphene-molecular imprinted polymers composite recognition element, Biosensors & Bioelectronics 28(1) (2011) 291-297. https://doi.org/10.1016/j.bios.2011.07.034.

[30] Q. Wu, M. Li, Z. Huang, Y. Shao, L. Bai, L. Zhou, Well-defined nanostructured core-shell magnetic surface imprinted polymers (Fe3O4@SiO2@MIPs) for effective extraction of trace tetrabromobisphenol A from water, Journal of Industrial and Engineering Chemistry 60 (2018) 268-278. https://doi.org/10.1016/j.jiec.2017.11.013.

[31] Y. Liu, Q. Liu, J. Li, H.H. Ngo, W. Guo, J. Hu, M.T. Gao, Q. Wang, Y. Hou, Effect of magnetic powder on membrane fouling mitigation and microbial community/composition in membrane bioreactors (MBRs) for municipal wastewater treatment, Bioresour Technol 249 (2018) 377-385. https://doi.org/10.1016/j.biortech.2017.10.027.

[32] C. Roggo, E. Coronado, S.K. Moreno-Forero, K. Harshman, J. Weber, J.R. van der Meer, Genome-wide transposon insertion scanning of environmental survival functions in the polycyclic aromatic hydrocarbon degrading bacterium Sphingomonas wittichii RW1, Environmental Microbiology 15(10) (2013) 2681-2695. https://doi.org/10.1111/1462-2920.12125.

[33] Z. Zhang, H. Wang, H. Wang, C. Wu, M. Li, L. Li, Fabrication and evaluation of molecularly imprinted magnetic nanoparticles for selective recognition and magnetic separation of lysozyme in human urine, Analyst 143(23) (2018) 5849-5856. https://doi.org/10.1039/c8an01746h.

[34] J. Kim, Y. Piao, N. Lee, Y.I. Park, I.-H. Lee, J.-H. Lee, S.R. Paik, T. Hyeon, Magnetic Nanocomposite Spheres Decorated with NiO Nanoparticles for a Magnetically Recyclable Protein Separation System, Adv Mater 22(1) (2010) 57-+. https://doi.org/10.1002/adma.200901858.

[35] X. Kan, Y. Zhao, Z. Geng, Z. Wang, J.-J. Zhu, Composites of multiwalled carbon nanotubes and molecularly imprinted polymers for dopamine recognition, Journal of Physical Chemistry C 112(13) (2008) 4849-4854. https://doi.org/10.1021/jp077445v.

[36] X. Wang, Q. Kang, D. Shen, Z. Zhang, J. Li, L. Chen, Novel monodisperse molecularly imprinted shell for estradiol based on surface imprinted hollow vinyl-SiO2 particles, Talanta 124 (2014) 7-13. https://doi.org/10.1016/j.talanta.2014.02.040.

[37] M.O. Miranda, W.E.C. Cavalcanti, F.F. Barbosa, J.A. De Sousa, F.I. Da Silva, S.B.C. Pergher, T.P. Braga, Photocatalytic degradation of ibuprofen using titanium oxide: insights into the mechanism and preferential attack of radicals, Rsc Advances 11(44) (2021) 27720-27733. https://doi.org/10.1039/d1ra04340d.

[38] C. Ku, P.H.L. Sit, Ab Initio Study of Electron and Hole Polaron Transport in Cobalt(II,III) Oxide Using Oxidation State Constrained Density Functional Theory, Journal of Physical Chemistry C 127(27) (2023) 13266-13275. https://doi.org/10.1021/acs.jpcc.3c02220.

[39] G. Su, L. Liu, L. Zhang, X. Liu, J. Xue, A. Tang, Fabrication of magnetic Fe3O4@SiO2@Bi2O2CO3/rGO composite for enhancing its photocatalytic performance for organic dyes and recyclability, Environmental Science and Pollution Research 28(36) (2021) 50286-50301. https://doi.org/10.1007/s11356-021-14248-z.

[40] Z. Zhang, L. Li, H. Wang, L. Guo, Y. Zhai, J. Zhang, Y. Yang, H. Wang, Z. Yin, Y. Lu, Preparation of molecularly imprinted ordered mesoporous silica for rapid and selective separation of trace bisphenol A from water samples, Applied Surface Science 448 (2018) 380-

388. https://doi.org/10.1016/j.apsusc.2018.04.017.

[41] J. Li, B. Jiang, Y. Liu, C. Qiu, J. Hu, G. Qian, W. Guo, H.H. Ngo, Preparation and adsorption properties of magnetic chitosan composite adsorbent for Cu^{2+} removal, J Cleaner Prod 158 (2017) 51-58. https://doi.org/https://doi.org/10.1016/j.jclepro.2017.04.156.

[42] S. Khan, S. Hussain, A. Wong, M.V. Foguel, L. Moreira Gonçalves, M.I. Pividori Gurgo, M.d.P. Taboada Sotomayor, Synthesis and characterization of magnetic-molecularly imprinted polymers for the HPLC-UV analysis of ametryn, Reactive and Functional Polymers 122 (2018) 175-182. https://doi.org/https://doi.org/10.1016/j.reactfunctpolym.2017.11.002.

[43] Z. Zhang, X. Zhang, D. Niu, Y. Li, J. Shi, Large-pore, silica particles with antibody-like, biorecognition sites for efficient protein separation, Journal of Materials Chemistry B 5(22) (2017) 4214-4220. https://doi.org/10.1039/c7tb00886d.

[44] A. Belayachi, B. Bestani, A. Benderdua, N. Benderdouche, L. Duclaux, The influence of surface functionalization of activated carbon on dyes and metal ion removal from aqueous media, Desalination and Water Treatment 57(37) (2016) 17557-17569. https://doi.org/10.1080/19443994.2015.1086701.

[45] C. Mahamadi, T. Nharingo, Utilization of water hyacinth weed (Eichhornia crassipes) for the removal of Pb(II), Cd(II) and Zn(II) from aquatic environments: an adsorption isotherm study, Environmental Technology 31(11) (2010) 1221-1228. https://doi.org/10.1080/09593331003646604.

[46] N. Kumar, N. Narayanan, S. Gupta, Application of magnetic molecularly imprinted polymers for extraction of imidacloprid from eggplant and honey, Food Chemistry 255 (2018)

81-88. https://doi.org/https://doi.org/10.1016/j.foodchem.2018.02.061.

[47] B. Liu, M. Han, G. Guan, S. Wang, R. Liu, Z. Zhang, Highly-Controllable Molecular Imprinting at Superparamagnetic Iron Oxide Nanoparticles for Ultrafast Enrichment and Separation, Journal of Physical Chemistry C 115(35) (2011) 17320-17327. https://doi.org/10.1021/jp205327q.